

JOLT3D: Joint Learning of Talking Heads and 3DMM Parameters with Application to Lip-Sync

Sungjoon Park
fatrat@snu.ac.kr

Hudson AI
Seoul, KR

Minsik Park
mspark@hudson-ai.com

Haneol Lee
haneol.lee@hudson-ai.com

Jaesub Yun
jaesub.yun@hudson-ai.com

Donggeon Lee
donggeon.lee@hudson-ai.com

Abstract

In this work, we revisit the effectiveness of 3DMM for talking head synthesis by jointly learning a 3D face reconstruction model and a talking head synthesis model. This enables us to obtain a FACS-based blendshape representation of facial expressions that is optimized for talking head synthesis. This contrasts with previous methods that either fit 3DMM parameters to 2D landmarks or rely on pretrained face reconstruction models. Not only does our approach increase the quality of the generated face, but it also allows us to take advantage of the blendshape representation to modify just the mouth region for the purpose of audio-based lip-sync. To this end, we propose a novel lip-sync pipeline that, unlike previous methods, decouples the original chin contour from the lip-synced chin contour, and reduces flickering near the mouth. Project page: <https://park-sungjoon.github.io/jolt3d/>

Introduction

The 3D morphable face model (3DMM) [1] is an important and widely used tool for modeling the human face. With the advent of deep learning, the task of monocular 3D face reconstruction from in-the-wild face images using the 3DMM has been extensively studied [2, 3, 8, 32, 58]. This has motivated the use of 3DMMs for talking head synthesis (THS). Although many efforts have been made in this direction, the idea has not gained popularity. This is because existing approaches typically extract the 3DMM parameters either via landmark fitting [9, 69, 77] or through pretrained models [26, 47, 61, 63, 66, 70, 71, 72, 75]. The former approach is inherently limited, as 2D landmarks cannot fully capture the 3D

geometry of the face. This limitation is exacerbated by the fact that off-the-shelf landmark detectors are often trained on noisy human-annotated labels. The latter approach is constrained by the quality of pretrained 3D face reconstruction models—referred to as ReconNet in this work—which may not yield satisfactory results. In particular, off-the-shelf ReconNets [6, 8, 16] are typically trained using photometric losses by utilizing the texture map of the Basel Face Model [18, 22]. This is suboptimal because these 3DMM parameters are not optimized for THS, and the texture map of the Basel Face Model cannot accurately capture the facial attributes.

Moreover, using a pretrained ReconNet limits the flexibility of adopting a different 3DMM than the one it was originally trained with. This is because one must not only retrain the ReconNet, but also consider the fact that not all 3DMMs come with a texture map. Popular ReconNets such as D3DFR [8], DECA [16], and EMOCA [8] are based on FLAME [3] or FaceWarehouse [10]. However, the expression parameters of FLAME are hard to interpret because they are generated by PCA. Since there are many alternatives to the 3DMM for encoding the facial attributes, such as neural embeddings [10, 12, 18] or keypoints [20, 22, 23], FLAME offers limited advantage over these alternatives. The FaceWarehouse uses blendshapes based on Facial Action Coding System [14] (FACS), but does not have eyeball mesh, which makes gaze control difficult without additional modeling.

In this work, we propose to jointly train the ReconNet and the THS model. To the best of our knowledge, this is the first effort towards training a ReconNet that is optimized for THS. Instead of using FLAME or FaceWarehouse, we adopt the ICT-FaceKit [22], which has 55 blendshapes (compared to 46 in FaceWarehouse) and includes eyeball geometry. We prefer ICT-FaceKit because the FACS-based blendshapes enable intuitive control of the face. The eyeballs also allow gaze control without additional modeling [10]. Although ICT-FaceKit lacks a texture map, this is not a hindrance due to our training strategy. We therefore free 3DMM-based THS from the limitations outlined above.

Thanks to the disentangled control of facial regions enabled by FACS-based blendshapes, it is possible to modify only the mouth-related blendshapes for lip-sync applications. For this, we train a model to predict mouth blendshapes from audio and talking style using a diffusion model [24, 24, 25]. The face generated by using these mouth blendshapes can then be blended into the original video by a simple face blending network. However, blending the generated face into the original video is complicated by the choice of the mouth mask. Common approaches include masking the lower half of the face [45], using a fixed square region [28], or employing a mouth-shape-agnostic mask [31]. We find these strategies unsatisfactory, and propose instead to inpaint just the mouth region after modifying the chin contour of the original face, see Fig. 4 for an overview of the lip-sync pipeline.

The main contributions of this work are as follows:

- We propose JOLT3D, a novel framework where ReconNet is optimized for THS.
- We achieve disentangled control over FACS-based blendshapes, including gaze.
- We propose a novel lip-sync pipeline that avoids the common mouth-mask artifacts.

2 Related works

2.1 Audio-driven talking head synthesis

Early works directly mapped audio to lip shapes by encoding and decoding the reference images and audio, constrained by a lip-sync loss [59, 41, 45, 60]. Other approaches predicted 3DMMs [76, 69, 73, 75, 77] or facial landmarks [50] from audio for THS. Recent methods use diffusion models to predict various forms of facial representations from audio [28, 51, 52, 53, 54] for THS. In our work, 3DMM is used as the facial representation for THS, and diffusion model is used to predict the 3DMM parameters from audio and talking style.

2.2 Talking head synthesis based on feature warping

In this family of methods, faces are generated by decoding the warped features extracted from reference images. Note that because convolution is translation-equivariant, smoothly varying warping fields tend to produce temporally consistent results. Some methods constrain the warping field to affine transformations [77, 28]. Implicit keypoints, which can be either 2D [27, 52] or 3D [70, 52, 75], are also commonly used to guide the warping process. Other approaches rely on dense warping fields, which can be either 2D [8, 10] or 3D [10, 10, 58]. The neural embeddings used in MegaPortraits [10] can capture detailed expressions [10], although it requires careful treatment of the latent vectors. Finally, some methods propose warping the features implicitly [38, 59].

In our work, we jointly train a ReconNet with a THS model that is based on dense 2D warping fields. This turns out to be very effective, and we expect that similar compatibility will hold for THS methods based on 3D warping fields.

2.3 Talking head synthesis that uses 3DMMs

While numerous studies use 3DMMs for THS, they typically either fit the 3DMM parameters to 2D facial landmarks [8, 59, 74], or use a pretrained ReconNet to extract the 3DMM parameters [74, 56, 61, 63, 66, 70, 71, 72, 73, 75]. In contrast, our approach jointly trains ReconNet with the talking head generator. This ensures that the 3DMM parameters are optimized for the task of THS.

3 Joint Training of ReconNet and Generator

The overview of our joint training scheme is shown in Fig. 1. The model architecture is similar to that of HeadGAN [8], but there are important differences that will be discussed below. For further details, please see the Supplementary Materials (SM).

3.1 Processing the 3DMM for talking head synthesis

The ICT-FaceKit contains many accessories that are superfluous for our purposes, so we retain only the face and eyeballs. Because the ICT-FaceKit does not define how the gaze blendshapes (eyeLookUp, eyeLookDown, eyeLookLeft, eyeLookRight) should be coupled to gaze directions, we define these relations ourselves, see SM for pseudocode.

Let M denote the face mesh and \mathbf{c} the projective camera parameters. To utilize 3DMM for THS, we render the mean face coordinates $P = \text{Renderer}(M, \mathbf{c})$, similarly to [8, 52], using

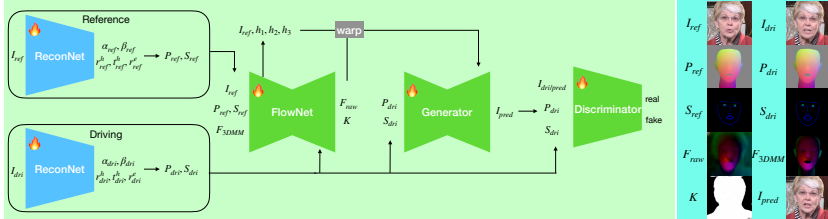


Figure 1: Joint training of ReconNet and Generator. The ReconNet extracts 3DMM parameters from the reference (I_{ref}) and the driving (I_{dri}) images. These parameters are encoded into $P_{ref/dri}$, $S_{ref/dri}$, and F_{3DMM} . FlowNet takes I_{ref} , P_{ref} , S_{ref} , and F_{3DMM} as inputs to predict the raw flow field F_{raw} and the mask K . I_{ref} and the intermediate features of FlowNet (h_i) are then warped. The Generator takes P_{dri} , S_{dri} , and the warped features to predict the driving face image I_{dri}^{pred} . The Discriminator receives either I_{pred} or I_{dri} , along with S_{dri} and P_{dri} , to determine whether the image looks realistic.

PyTorch3D [46]. We also draw sketch S of the face using a two-channel representation: one for the overall face and one for the iris. We also compute the 2D flow field F_{3DMM} resulting from the changes in 3DMM parameters by calculating how the projected vertex coordinates shift between the reference and target faces, see Fig. 1 for visualization.

3.2 Pretraining the ReconNet

For stable joint training, we pretrain the ReconNet using facial landmarks. The ReconNet outputs α , β , r^h , t^h , r^e , where α is the identity, β is the blendshape, r^h and t^h are the head rotation and translation, and r^e is the eyeball rotation. The ReconNet is trained to fit the projected 3DMM vertices to 2D landmark labels obtained from off-the-shelf landmark detectors [19]. We use L2 loss for landmarks and apply L2 regularization for identity and blendshapes. We also include L2 loss between α 's extracted from two different images of a person for identity consistency, and constrain the blendshapes to lie between 0 and 1.

3.3 Joint training of ReconNet and the Generator

We modify the feature warping mechanism of HeadGAN, which is unstable. In the original formulation, FlowNet predicts the mask K , which determines where to apply the warping, and the raw flow field F_{raw} . Then, the flow field and the warped image are computed as:

$$F = K F_{raw}, \quad I_{warped} = F \star I. \quad (1)$$

The multiplication in the first equation is element-wise, and \star denotes the warping operation. We find that K can collapse to 0 during training, that is, $F = 0$. We hypothesize that this is because (1) Initially, it is difficult to learn F because the Generator does not produce a meaningful face. (2) As a result, it is easy for the Generator to rely on S_{dri} and P_{dri} for the face shape, and the unwarped features for the face and background textures. (3) Once $K = 0$, training gets stuck because the magnitude of F is determined by both F_{raw} (linear activation) and K (sigmoid activation). We therefore decouple magnitude of flow from K as follows:

$$I_{warped} = K(F_{raw} \star I) + (1 - K)I. \quad (2)$$

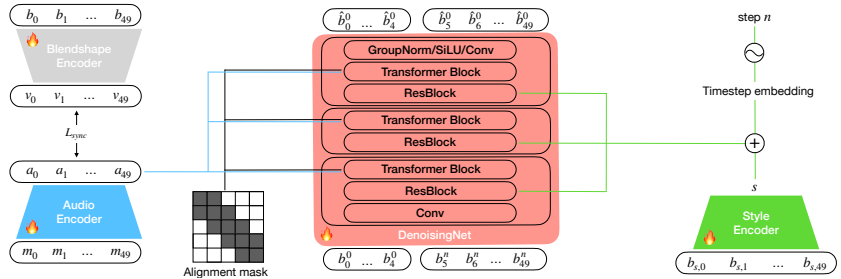


Figure 2: The Audio-to-Blendshape model. The Blendshape Encoder is an auxiliary model for computing the sync-loss, and is not used during inference.

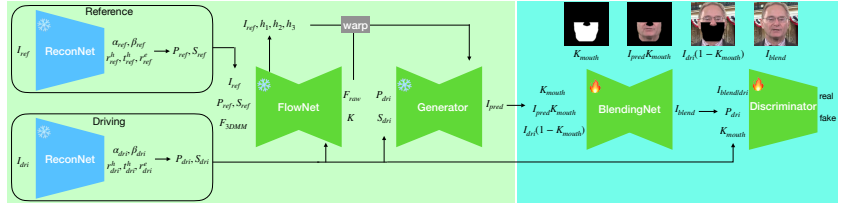


Figure 3: BlendingNet takes the mouth region of the predicted face, the region outside the mouth of the original face, and the mouth mask to predict the blended face.

For joint training, we add to the losses in Sec. 3.2 the standard photometric losses and the GAN losses. For spatial locality of mouth blendshapes, we generate face after modifying just the mouth blendshapes, and impose L1 pixel loss on changes that occur outside the mouth region. To prevent head pose or expression from leaking into the α , we randomly swap the identity parameters between the driving and the reference. To prevent identity from leaking into β , we randomly shuffle blendshapes within the batch and impose cosine similarity between the ArcFace [7] embeddings of the original and the generated face.

4 Application to Lip-Sync

4.1 Audio-to-Blendshape

For lip-sync, we train a diffusion model [40, 51] to predict the 35 mouth blendshapes (shown in Fig. 5) from audio and talking style embeddings, see Fig. 2.

First, note that the video is set to 25 fps and audio is sampled at 16 kHz. To compute the audio embeddings, we take 2s of audio and compute the Mel spectrogram with 80 frequency bins and a hop size of 200. The Mel spectrogram is split into 50 equally-spaced overlapping chunks $m_i \in \mathbb{R}^{16 \times 80}$. The Audio Encoder encodes m_i into $a_i \in \mathbb{R}^{512}$, $i = 0, \dots, 49$. To capture the speaking style, we sample 50 consecutive mouth blendshapes $b_{s,i} \in \mathbb{R}^{35}$, $i = 0, \dots, 49$ (spanning 2s) from a different part of the video. The Style Encoder encodes $b_{s,i}$ into $s \in \mathbb{R}^{512}$.

The DenoisingNet \mathcal{N} transforms noise into mouth blendshapes, conditioned on a_i and s . Let b_i , $i = 0, \dots, 49$ be the mouth blendshapes corresponding to a_i . The first five blendshapes are used to provide the temporal context to \mathcal{N} , enabling it to generate a continuous blendshape sequence. For the remaining blendshapes, \mathcal{N} is used to transform the noisy blendshapes b^n into denoised blendshapes as $\hat{b}^0 = \mathcal{N}(b_{0:4}, b_{5:49}^n, a_{0:49}, n)$. Here, n is the time

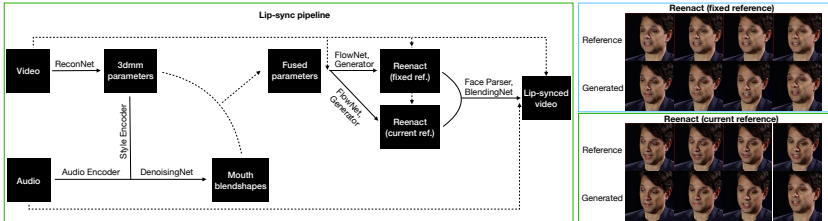


Figure 4: Left: lip-sync pipeline. Right: reenactment with fixed and current references.

step in the denoising process with the convention that $n = 0$ corresponds to the original distribution and $n = T$ corresponds to pure noise.

We train using the denoising loss, supplemented by velocity and smoothness losses. To help train the Audio Encoder, we use the Blendshape Encoder to encode the blendshapes b_i corresponding to a_i into v_i , and compute the sync-loss between them (see SM for details).

4.2 Face Blending

As will be detailed in Sec. 4.3, a difficulty with lip-syncing is that only the mouth region should be changed. We approach this problem by first training a neural net that blends the face that is generated from a fixed reference frame into the original video. For simplicity, we train a UNet \mathcal{B} using the GAN framework (see Fig. 3).

Let I_{dri} be the original image, K_{mouth} the mouth segmentation map, and I_{pred} the predicted image. The blended image is given by $I_{blend} = \mathcal{B}(I_{dri}(1 - K_{mouth}), K_{mouth}, I_{pred}K_{mouth})$. The network is trained using photometric and GAN losses.

4.3 Full Lip-Sync Pipeline

Our lip-sync (dubbing) pipeline is shown in Fig. 4. We assume that the face to be lip-synced has been detected and that the dubbing audio is provided. We begin by cropping the face from the video and extracting the 3DMM parameters using the ReconNet. Next, we extract the style and audio embeddings, which are used to predict denoised mouth blendshapes \hat{b} . These mouth blendshapes \hat{b} are inserted into the 3DMM parameters extracted from the original video. Using the fused 3DMM parameters, we reenact the (cropped) face twice: (1) with a fixed reference frame to obtain I_{FF} , and (2) with the current frame I_{CF} (see Fig. 4). We extract the mouth region from I_{CF} , and blend I_{FF} into I_{CF} . The blended face is then composited back into the original video.

We now explain the rationale behind generating the face twice to obtain I_{FF} and I_{CF} . As can be expected, simply inpainting the mouth region of the original face using I_{FF} yields unsatisfactory results since the chin contour cannot be modified. On the other hand, inpainting a large, mouth-shape-agnostic region using I_{FF} can result in noticeable flickering, especially when the neighboring regions of the mask differ between the reference and the current frame. Using the current frame as the reference also results in unnatural video because the reference frame keeps changing. We resolve this difficulty by first adjusting the face contour appropriately to obtain I_{CF} , and then blending in I_{FF} . This can also enhance video consistency, especially when teeth are visible in the fixed reference frame.



Figure 5: Responses to changes in blendshapes. The mouth blendshapes are highlighted.



Figure 6: Results of self-reenactment (above) and cross-reenactment (below).



Figure 7: First row: Large mouth mask in LatentSync can cause flickering near the mouth. Second and third rows: MuseTalk and JoyGen cannot change the chin contour, causing face shape to change. Our approach does show these problems.

5 Experiments

5.1 Dataset

We use various publicly available datasets: AVSpeech [15], VoxCeleb2 [8], CelebV-HQ [33], TalkingHead-1KH [16], and VFHQ [35]. We use the topiq_nr-face metric in pyiqa [8, 1] to filter out faces with quality lower than 0.4. Since audio-visual correlation is important for training the Audio-to-Blendshape model, we restore the sync, and remove data with probability-at-offset < 0.8 or offscreen ratio > 0.354 [40].

5.2 FACS based Blendshapes

In Fig. 5, we show that, in many cases, the generated face responds to changes in blendshapes as expected. However, the model does not respond adequately to blendshapes such as `cheekPuff`. We hypothesize that this is due to the use of 2D warping fields and the absence of multi-view consistency during training.

5.3 Self-reenactment and cross-reenactment

In Table 1 and Fig. 6, we compare our method on the task of facial expression transfer with representative THS methods that utilize 3DMM. For evaluation, we randomly sample 52 videos from the HDTF dataset, and parts of the VoxCeleb2 dataset (about 1 hour) that are not used for training. We compute L1, PSNR, SSIM, and FID [22] to evaluate image quality. We compute lip-sync metrics LSE-D and LSE-C [35] to evaluate mouth shape quality, and compute CSIM [10] to evaluate identity preservation. Our method outperforms others in most cases, both qualitatively and quantitatively, see SM for more details.

5.4 Lip-Syncing

In Table 2, we compare our method with LatentSync [31], MuseTalk [76], and JoyGen [61] on the task of lip-sync. LatentSync outperforms other methods in terms of the LSE-D and LSE-C metrics. One reason behind this is that LatentSync directly optimizes the sync-loss.

Table 1: Evaluation metrics for self-reenactment and cross-reenactment.

Method	L1↓	PSNR↑	SSIM↑	FID↓	LSE-D↓	LSE-C↑	CSIM↑
HDTF dataset							
Real3D-Portrait [69]	8.81	22.8	0.822	24.1, 48.3	8.12, 8.42	6.71, 6.45	0.912, 0.887
HeadGAN [8]	8.90	22.6	0.787	20.5, 47.0	7.79, 9.10	7.06, 5.61	0.907, 0.791
FADM [20]	7.20	25.5	0.855	16.4, 46.4	8.12, 8.96	6.69, 5.94	0.931, 0.845
Ours	5.18	27.7	0.891	11.3, 43.9	7.02, 7.83	8.12, 7.21	0.949, 0.833
VoxCeleb2 dataset							
Real3D-Portrait [69]	12.2	21.1	0.799	17.1, 19.5	9.00, 9.42	4.66, 4.22	0.832, 0.808
HeadGAN [8]	12.1	21.4	0.742	13.1, 24.9	8.51, 9.26	5.11, 4.22	0.795, 0.442
FADM [20]	9.97	23.9	0.817	9.97, 23.1	9.07, 9.88	4.46, 3.63	0.882, 0.624
Ours	7.42	25.7	0.852	7.19, 24.9	7.90, 8.62	5.94, 5.12	0.912, 0.652

Table 2: Evaluation metrics for lip-sync with original and different audio.

Method	FID↓	LSE-D↓	LSE-C ↑	CSIM↑	ACL↑
HDTF dataset					
LatentSync [31]	4.05, 11.4	5.78, 6.00	9.76, 9.41	0.967, 0.962	1.04, 1.26
MuseTalk [73]	4.76, 11.9	8.30, 10.8	6.64, 4.09	0.967, 0.965	0.882, 0.957
JoyGen [61]	8.87, 18.0	7.19, 8.90	7.89, 5.90	0.971, 0.968	0.832, 0.926
Ours blended	3.51, 10.5	8.26, 8.99	6.58, 5.80	0.972, 0.967	1.08, 1.32
VoxCeleb2 dataset					
LatentSync [31]	2.15, 3.22	6.41, 6.84	7.94, 7.21	0.964, 0.953	1.04, 1.19
MuseTalk [73]	2.93, 3.81	8.58, 10.7	5.11, 2.88	0.918, 0.910	1.03, 1.05
JoyGen [61]	5.14, 6.74	7.72, 9.54	6.10, 4.16	0.938, 0.927	1.02, 1.06
Ours blended	1.91, 2.85	9.57, 9.57	3.93, 3.93	0.965, 0.959	1.17, 1.33

In fact, it achieves better lip-sync metrics even than the original videos, for which LSE-D is 6.8948 (HDTF) and 7.68 (VoxCeleb2), and LSE-C is 8.22 (HDTF) and 6.12 (VoxCeleb2).

Although our method does not achieve the best LSE-D and LSE-C, it reduces visual artifacts (see Fig. 7). LatentSync uses a large, mouth-shape-agnostic mask, and inpaints the masked region. As can be seen, this can lead to flickering when the visual pattern near the mouth is complex. In contrast, our approach does not suffer from such artifacts.

Another common artifact of lip-synced videos is the preservation of the original chin contour. The source of the issue lies in the masking strategy. For example, MuseTalk and JoyGen inpaint the lower part of the face using a rectangular mask. This causes the model to associate the chin contour with the mask size. As a result, the chin line of the original video is preserved in the lip-synced video, which causes lengthening or shortening of the face. This is not an issue when our lip-sync pipeline is adopted because we modify the original chin contour before blending in the lip-synced face. To quantitatively evaluate this, we define the metric $\Delta CL = \frac{|y_{2,orig} - y_{2,lipsync}|}{y_{2,orig} - y_{1,orig}}$. Here, y_1 and y_2 are the top and bottom coordinates of face bounding box, and the subscripts orig and lipsync indicate original and lip-synced results, respectively. As shown in Table 2 and Fig. 7, MuseTalk and JoyGen fail to modify the chin line, and the correlation persists in LatentSync as well because the mouth mask cannot completely eliminate information on the original mouth shape.

6 Conclusion

Contrary to common belief, we have shown that 3DMM remains a suitable representation for the purpose of THS. The limitations of previous approaches that rely on 3DMM stem from poor extraction of 3DMM parameters, rather than from limitations of 3DMM itself. Using the FACS-based blendshapes of ICT-FaceKit, we have also proposed a lip-sync pipeline that allows modification of the chin contour and reduces flickering near the mouth.

The fact that warping-field-based approaches to THS are highly compatible with the joint learning of ReconNet has important implications. For example, our method can readily be generalized to approaches using 3D warping fields such as face-vid2vid [6] by binding 3D keypoints to vertices of the 3DMM. It would also be interesting to explore whether keypoints can be bound to the 3DMM to control the tongue movement, or whether the 3DMM can be supplemented with additional latent vectors that capture fine-grained facial details, such as wrinkles. We leave the answers to these questions for future research.

References

- [1] Chen Cao, Yanlin Weng, Shun Zhou, Yiyi Tong, and Kun Zhou. Facewarehouse: A 3d facial expression database for visual computing. *IEEE Transactions on Visualization and Computer Graphics*, 20(3):413–425, 2013.
- [2] Zenghao Chai, Tianke Zhang, Tianyu He, Xu Tan, Tadas Baltrusaitis, HsiangTao Wu, Runnan Li, Sheng Zhao, Chun Yuan, and Jiang Bian. Hiface: High-fidelity 3d face reconstruction by learning static and dynamic details. In *Proceedings of the IEEE/CVF International Conference on Computer Vision*, pages 9087–9098, 2023.
- [3] Chaofeng Chen and Jiadi Mo. IQA-PyTorch: Pytorch toolbox for image quality assessment. [Online]. Available: <https://github.com/chaofengc/IQA-PyTorch>, 2022.
- [4] Chaofeng Chen, Jiadi Mo, Jingwen Hou, Haoning Wu, Liang Liao, Wenxiu Sun, Qiong Yan, and Weisi Lin. Topiq: A top-down approach from semantics to distortions for image quality assessment. *IEEE Transactions on Image Processing*, 2024.
- [5] Joon Son Chung, Arsha Nagrani, and Andrew Zisserman. Voxceleb2: Deep speaker recognition. *arXiv preprint arXiv:1806.05622*, 2018.
- [6] Radek Daněček, Michael J Black, and Timo Bolkart. Emoca: Emotion driven monocular face capture and animation. In *Proceedings of the IEEE/CVF Conference on Computer Vision and Pattern Recognition*, pages 20311–20322, 2022.
- [7] Jiankang Deng, Jia Guo, Niannan Xue, and Stefanos Zafeiriou. Arcface: Additive angular margin loss for deep face recognition. In *Proceedings of the IEEE/CVF conference on computer vision and pattern recognition*, pages 4690–4699, 2019.
- [8] Yu Deng, Jiaolong Yang, Sicheng Xu, Dong Chen, Yunde Jia, and Xin Tong. Accurate 3d face reconstruction with weakly-supervised learning: From single image to image set. In *Proceedings of the IEEE/CVF conference on computer vision and pattern recognition workshops*, pages 0–0, 2019.

[9] Michail Christos Doukas, Stefanos Zafeiriou, and Viktoriia Sharmanska. Headgan: One-shot neural head synthesis and editing. In *Proceedings of the IEEE/CVF International conference on Computer Vision*, pages 14398–14407, 2021.

[10] Michail Christos Doukas, Evangelos Ververas, Viktoriia Sharmanska, and Stefanos Zafeiriou. Free-headgan: Neural talking head synthesis with explicit gaze control. *IEEE Transactions on Pattern Analysis and Machine Intelligence*, 45(8):9743–9756, 2023.

[11] Nikita Drobyshev, Jenya Chelishev, Taras Khakhulin, Aleksei Ivakhnenko, Victor Lem-pitsky, and Egor Zakharov. Megaportraits: One-shot megapixel neural head avatars. In *Proceedings of the 30th ACM International Conference on Multimedia*, pages 2663–2671, 2022.

[12] Nikita Drobyshev, Antoni Bigata Casademunt, Konstantinos Vougioukas, Zoe Landgraf, Stavros Petridis, and Maja Pantic. Emoportraits: Emotion-enhanced multimodal one-shot head avatars. In *Proceedings of the IEEE/CVF Conference on Computer Vision and Pattern Recognition*, pages 8498–8507, 2024.

[13] Bernhard Egger, William AP Smith, Ayush Tewari, Stefanie Wuhrer, Michael Zollhoefer, Thabo Beeler, Florian Bernard, Timo Bolkart, Adam Kortylewski, Sami Romdhani, et al. 3d morphable face models—past, present, and future. *ACM Transactions on Graphics (ToG)*, 39(5):1–38, 2020.

[14] Paul Ekman and Wallace V Friesen. Facial action coding system. *Environmental Psychology & Nonverbal Behavior*, 1978.

[15] Ariel Ephrat, Inbar Mosseri, Oran Lang, Tali Dekel, Kevin Wilson, Avinatan Hassidim, William T Freeman, and Michael Rubinstein. Looking to listen at the cocktail party: A speaker-independent audio-visual model for speech separation. *arXiv preprint arXiv:1804.03619*, 2018.

[16] Yao Feng, Haiwen Feng, Michael J Black, and Timo Bolkart. Learning an animatable detailed 3d face model from in-the-wild images. *ACM Transactions on Graphics (ToG)*, 40(4):1–13, 2021.

[17] Michael Garland and Paul S Heckbert. Surface simplification using quadric error metrics. In *Proceedings of the 24th annual conference on Computer graphics and interactive techniques*, pages 209–216, 1997.

[18] Thomas Gerig, Andreas Morel-Forster, Clemens Blumer, Bernhard Egger, Marcel Luthi, Sandro Schönborn, and Thomas Vetter. Morphable face models—an open framework. In *2018 13th IEEE international conference on automatic face & gesture recognition (FG 2018)*, pages 75–82. IEEE, 2018.

[19] Ivan Grishchenko, Artsiom Ablavatski, Yury Kartynnik, Karthik Raveendran, and Matthias Grundmann. Attention mesh: High-fidelity face mesh prediction in real-time. *arXiv preprint arXiv:2006.10962*, 2020.

[20] Jianzhu Guo, Dingyun Zhang, Xiaoqiang Liu, Zhizhou Zhong, Yuan Zhang, Pengfei Wan, and Di Zhang. Liveportrait: Efficient portrait animation with stitching and retargeting control. *arXiv preprint arXiv:2407.03168*, 2024.

- [21] Kaiming He, Xiangyu Zhang, Shaoqing Ren, and Jian Sun. Deep residual learning for image recognition. In *Proceedings of the IEEE conference on computer vision and pattern recognition*, pages 770–778, 2016.
- [22] Martin Heusel, Hubert Ramsauer, Thomas Unterthiner, Bernhard Nessler, and Sepp Hochreiter. Gans trained by a two time-scale update rule converge to a local nash equilibrium. *Advances in neural information processing systems*, 30, 2017.
- [23] Jonathan Ho and Tim Salimans. Classifier-free diffusion guidance. *arXiv preprint arXiv:2207.12598*, 2022.
- [24] Jonathan Ho, Ajay Jain, and Pieter Abbeel. Denoising diffusion probabilistic models. *Advances in neural information processing systems*, 33:6840–6851, 2020.
- [25] Phillip Isola, Jun-Yan Zhu, Tinghui Zhou, and Alexei A Efros. Image-to-image translation with conditional adversarial networks. In *Proceedings of the IEEE conference on computer vision and pattern recognition*, pages 1125–1134, 2017.
- [26] Xiaozhong Ji, Chuming Lin, Zhonggan Ding, Ying Tai, Junwei Zhu, Xiaobin Hu, Donghao Luo, Yanhao Ge, and Chengjie Wang. Realtalk: Real-time and realistic audio-driven face generation with 3d facial prior-guided identity alignment network. *arXiv preprint arXiv:2406.18284*, 2024.
- [27] Xinya Ji, Hang Zhou, Kaisiyuan Wang, Qianyi Wu, Wayne Wu, Feng Xu, and Xun Cao. Eamm: One-shot emotional talking face via audio-based emotion-aware motion model. In *ACM SIGGRAPH 2022 conference proceedings*, pages 1–10, 2022.
- [28] Jianwen Jiang, Chao Liang, Jiaqi Yang, Gaojie Lin, Tianyun Zhong, and Yanbo Zheng. Loopy: Taming audio-driven portrait avatar with long-term motion dependency. In *The Thirteenth International Conference on Learning Representations*, 2024.
- [29] Diederik P Kingma and Jimmy Ba. Adam: A method for stochastic optimization. *arXiv preprint arXiv:1412.6980*, 2014.
- [30] Christian Ledig, Lucas Theis, Ferenc Huszár, Jose Caballero, Andrew Cunningham, Alejandro Acosta, Andrew Aitken, Alykhan Tejani, Johannes Totz, Zehan Wang, et al. Photo-realistic single image super-resolution using a generative adversarial network. In *Proceedings of the IEEE conference on computer vision and pattern recognition*, pages 4681–4690, 2017.
- [31] Chunyu Li, Chao Zhang, Weikai Xu, Jinghui Xie, Weiguo Feng, Bingyue Peng, and Weiwei Xing. Latentsync: Audio conditioned latent diffusion models for lip sync. *arXiv preprint arXiv:2412.09262*, 2024.
- [32] Rui long Li, Karl Bladin, Yajie Zhao, Chinmay Chinara, Owen Ingraham, Pengda Xiang, Xinglei Ren, Pratusha Prasad, Bipin Kishore, Jun Xing, et al. Learning formation of physically-based face attributes. In *Proceedings of the IEEE/CVF conference on computer vision and pattern recognition*, pages 3410–3419, 2020.
- [33] Jae Hyun Lim and Jong Chul Ye. Geometric gan. *arXiv preprint arXiv:1705.02894*, 2017.

[34] Shanchuan Lin, Linjie Yang, Imran Saleemi, and Soumyadip Sengupta. Robust high-resolution video matting with temporal guidance. In *Proceedings of the IEEE/CVF Winter Conference on Applications of Computer Vision*, pages 238–247, 2022.

[35] Tao Liu, Feilong Chen, Shuai Fan, Chenpeng Du, Qi Chen, Xie Chen, and Kai Yu. Anitalker: animate vivid and diverse talking faces through identity-decoupled facial motion encoding. In *Proceedings of the 32nd ACM International Conference on Multimedia*, pages 6696–6705, 2024.

[36] Ilya Loshchilov and Frank Hutter. Decoupled weight decay regularization. *arXiv preprint arXiv:1711.05101*, 2017.

[37] Andreas Lugmayr, Martin Danelljan, Andres Romero, Fisher Yu, Radu Timofte, and Luc Van Gool. Repaint: Inpainting using denoising diffusion probabilistic models. In *Proceedings of the IEEE/CVF conference on computer vision and pattern recognition*, pages 11461–11471, 2022.

[38] Arun Mallya, Ting-Chun Wang, and Ming-Yu Liu. Implicit warping for animation with image sets. *Advances in Neural Information Processing Systems*, 35:22438–22450, 2022.

[39] Urwa Muaz, Wondong Jang, Rohun Tripathi, Santhosh Mani, Wenbin Ouyang, Ravi Teja Gadde, Baris Gecer, Sergio Elizondo, Reza Madad, and Naveen Nair. Sidgan: High-resolution dubbed video generation via shift-invariant learning. In *Proceedings of the IEEE/CVF International Conference on Computer Vision*, pages 7833–7842, 2023.

[40] Inkyu Park and Jaewoong Cho. Said: Speech-driven blendshape facial animation with diffusion. *arXiv preprint arXiv:2401.08655*, 2023.

[41] Se Jin Park, Minsu Kim, Joanna Hong, Jeongsoo Choi, and Yong Man Ro. SyncTalk-face: Talking face generation with precise lip-syncing via audio-lip memory. In *Proceedings of the AAAI Conference on Artificial Intelligence*, volume 36, pages 2062–2070, 2022.

[42] Sungjoon Park, Jaesub Yun, Donggeon Lee, and Minsik Park. Interpretable convolutional syncnet. *arXiv preprint arXiv:2409.00971*, 2024.

[43] Taesung Park, Ming-Yu Liu, Ting-Chun Wang, and Jun-Yan Zhu. Semantic image synthesis with spatially-adaptive normalization. In *Proceedings of the IEEE/CVF conference on computer vision and pattern recognition*, pages 2337–2346, 2019.

[44] Pascal Paysan, Reinhard Knothe, Brian Amberg, Sami Romdhani, and Thomas Vetter. A 3d face model for pose and illumination invariant face recognition. In *2009 sixth IEEE international conference on advanced video and signal based surveillance*, pages 296–301. Ieee, 2009.

[45] KR Prajwal, Rudrabha Mukhopadhyay, Vinay P Namboodiri, and CV Jawahar. A lip sync expert is all you need for speech to lip generation in the wild. In *Proceedings of the 28th ACM international conference on multimedia*, pages 484–492, 2020.

[46] Nikhila Ravi, Jeremy Reizenstein, David Novotny, Taylor Gordon, Wan-Yen Lo, Justin Johnson, and Georgia Gkioxari. Accelerating 3d deep learning with pytorch3d. *arXiv:2007.08501*, 2020.

- [47] Yurui Ren, Ge Li, Yuanqi Chen, Thomas H Li, and Shan Liu. Pirenderer: Controllable portrait image generation via semantic neural rendering. In *Proceedings of the IEEE/CVF international conference on computer vision*, pages 13759–13768, 2021.
- [48] Olaf Ronneberger, Philipp Fischer, and Thomas Brox. U-net: Convolutional networks for biomedical image segmentation. In *Medical image computing and computer-assisted intervention–MICCAI 2015: 18th international conference, Munich, Germany, October 5-9, 2015, proceedings, part III 18*, pages 234–241. Springer, 2015.
- [49] Chitwan Saharia, William Chan, Huiwen Chang, Chris Lee, Jonathan Ho, Tim Salimans, David Fleet, and Mohammad Norouzi. Palette: Image-to-image diffusion models. In *ACM SIGGRAPH 2022 conference proceedings*, pages 1–10, 2022.
- [50] Tim Salimans, Ian Goodfellow, Wojciech Zaremba, Vicki Cheung, Alec Radford, and Xi Chen. Improved techniques for training gans. *Advances in neural information processing systems*, 29, 2016.
- [51] Maximilian Seitzer. pytorch-fid: FID Score for PyTorch. <https://github.com/mseitzer/pytorch-fid>, August 2020. Version 0.3.0.
- [52] Aliaksandr Siarohin, Stéphane Lathuilière, Sergey Tulyakov, Elisa Ricci, and Nicu Sebe. First order motion model for image animation. *Advances in neural information processing systems*, 32, 2019.
- [53] Karen Simonyan and Andrew Zisserman. Very deep convolutional networks for large-scale image recognition. *arXiv preprint arXiv:1409.1556*, 2014.
- [54] Jascha Sohl-Dickstein, Eric Weiss, Niru Maheswaranathan, and Surya Ganguli. Deep unsupervised learning using nonequilibrium thermodynamics. In *International conference on machine learning*, pages 2256–2265. pmlr, 2015.
- [55] Yang Song, Jascha Sohl-Dickstein, Diederik P Kingma, Abhishek Kumar, Stefano Ermon, and Ben Poole. Score-based generative modeling through stochastic differential equations. *arXiv preprint arXiv:2011.13456*, 2020.
- [56] Wenzhang Sun, Xiang Li, Donglin Di, Zhuding Liang, Qiyuan Zhang, Hao Li, Wei Chen, and Jianxun Cui. Uniavatar: Taming lifelike audio-driven talking head generation with comprehensive motion and lighting control. *arXiv preprint arXiv:2412.19860*, 2024.
- [57] Zhiyao Sun, Tian Lv, Sheng Ye, Matthieu Lin, Jenny Sheng, Yu-Hui Wen, Minjing Yu, and Yong-jin Liu. Diffposetalk: Speech-driven stylistic 3d facial animation and head pose generation via diffusion models. *ACM Transactions on Graphics (TOG)*, 43(4):1–9, 2024.
- [58] Ayush Tewari, Michael Zollhofer, Hyeongwoo Kim, Pablo Garrido, Florian Bernard, Patrick Perez, and Christian Theobalt. Mofa: Model-based deep convolutional face autoencoder for unsupervised monocular reconstruction. In *Proceedings of the IEEE international conference on computer vision workshops*, pages 1274–1283, 2017.
- [59] Dmitry Ulyanov, Andrea Vedaldi, and Victor Lempitsky. Instance normalization: The missing ingredient for fast stylization. *arXiv preprint arXiv:1607.08022*, 2016.

[60] Jiadong Wang, Xinyuan Qian, Malu Zhang, Robby T Tan, and Haizhou Li. Seeing what you said: Talking face generation guided by a lip reading expert. In *Proceedings of the IEEE/CVF Conference on Computer Vision and Pattern Recognition*, pages 14653–14662, 2023.

[61] Qili Wang, Daijiang Wu, Zihang Xu, Junshi Huang, and Jun Lv. Joygen: Audio-driven 3d depth-aware talking-face video editing. *arXiv preprint arXiv:2501.01798*, 2025.

[62] Ting-Chun Wang, Arun Mallya, and Ming-Yu Liu. One-shot free-view neural talking-head synthesis for video conferencing. In *Proceedings of the IEEE/CVF conference on computer vision and pattern recognition*, pages 10039–10049, 2021.

[63] Haozhe Wu, Jia Jia, Haoyu Wang, Yishun Dou, Chao Duan, and Qingshan Deng. Imitating arbitrary talking style for realistic audio-driven talking face synthesis. In *Proceedings of the 29th ACM International Conference on Multimedia*, pages 1478–1486, 2021.

[64] Yuxin Wu and Kaiming He. Group normalization. In *Proceedings of the European conference on computer vision (ECCV)*, pages 3–19, 2018.

[65] Liangbin Xie, Xintao Wang, Honglun Zhang, Chao Dong, and Ying Shan. Vfhq: A high-quality dataset and benchmark for video face super-resolution. In *Proceedings of the IEEE/CVF Conference on Computer Vision and Pattern Recognition*, pages 657–666, 2022.

[66] Chao Xu, Junwei Zhu, Jiangning Zhang, Yue Han, Wenqing Chu, Ying Tai, Chengjie Wang, Zhifeng Xie, and Yong Liu. High-fidelity generalized emotional talking face generation with multi-modal emotion space learning. In *Proceedings of the IEEE/CVF conference on computer vision and pattern recognition*, pages 6609–6619, 2023.

[67] Mingwang Xu, Hui Li, Qingkun Su, Hanlin Shang, Liwei Zhang, Ce Liu, Jingdong Wang, Yao Yao, and Siyu Zhu. Hallo: Hierarchical audio-driven visual synthesis for portrait image animation. *arXiv preprint arXiv:2406.08801*, 2024.

[68] Sicheng Xu, Guojun Chen, Yu-Xiao Guo, Jiaolong Yang, Chong Li, Zhenyu Zang, Yizhong Zhang, Xin Tong, and Baining Guo. Vasa-1: Lifelike audio-driven talking faces generated in real time. *Advances in Neural Information Processing Systems*, 37: 660–684, 2025.

[69] Zhenhui Ye, Tianyun Zhong, Yi Ren, Jiaqi Yang, Weichuang Li, Jiawei Huang, Ziyue Jiang, Jinzheng He, Rongjie Huang, Jinglin Liu, et al. Real3d-portrait: One-shot realistic 3d talking portrait synthesis. *arXiv preprint arXiv:2401.08503*, 2024.

[70] Zipeng Ye, Zhiyao Sun, Yu-Hui Wen, Yanan Sun, Tian Lv, Ran Yi, and Yong-Jin Liu. Dynamic neural textures: Generating talking-face videos with continuously controllable expressions. *arXiv preprint arXiv:2204.06180*, 2022.

[71] Ran Yi, Zipeng Ye, Juyong Zhang, Hujun Bao, and Yong-Jin Liu. Audio-driven talking face video generation with learning-based personalized head pose. *arXiv preprint arXiv:2002.10137*, 2020.

[72] Bohan Zeng, Xuhui Liu, Sicheng Gao, Boyu Liu, Hong Li, Jianzhuang Liu, and Baochang Zhang. Face animation with an attribute-guided diffusion model. In *Proceedings of the IEEE/CVF Conference on Computer Vision and Pattern Recognition*, pages 628–637, 2023.

[73] Chenxu Zhang, Yifan Zhao, Yifei Huang, Ming Zeng, Saifeng Ni, Madhukar Budagavi, and Xiaohu Guo. Facial: Synthesizing dynamic talking face with implicit attribute learning. In *Proceedings of the IEEE/CVF international conference on computer vision*, pages 3867–3876, 2021.

[74] Qiang Zhang, Tong Xiao, Haroun Habeeb, Larissa Laich, Sofien Bouaziz, Patrick Snape, Wenjing Zhang, Matthew Cioffi, Peizhao Zhang, Pavel Pidlypenskyi, et al. Refa: Real-time egocentric facial animations for virtual reality. In *Proceedings of the IEEE/CVF Conference on Computer Vision and Pattern Recognition*, pages 4793–4802, 2024.

[75] Wenzuan Zhang, Xiaodong Cun, Xuan Wang, Yong Zhang, Xi Shen, Yu Guo, Ying Shan, and Fei Wang. Sadtalker: Learning realistic 3d motion coefficients for stylized audio-driven single image talking face animation. In *Proceedings of the IEEE/CVF Conference on Computer Vision and Pattern Recognition*, pages 8652–8661, 2023.

[76] Yue Zhang, Minhao Liu, Zhaokang Chen, Bin Wu, Yubin Zeng, Chao Zhan, Yingjie He, Junxin Huang, and Wenjiang Zhou. Musetalk: Real-time high quality lip synchronization with latent space inpainting. *arXiv preprint arXiv:2410.10122*, 2024.

[77] Zhimeng Zhang, Lincheng Li, Yu Ding, and Changjie Fan. Flow-guided one-shot talking face generation with a high-resolution audio-visual dataset. In *Proceedings of the IEEE/CVF Conference on Computer Vision and Pattern Recognition*, pages 3661–3670, 2021.

[78] Zhimeng Zhang, Zhipeng Hu, Wenjin Deng, Changjie Fan, Tangjie Lv, and Yu Ding. Dinet: Deformation inpainting network for realistic face visually dubbing on high resolution video. In *Proceedings of the AAAI conference on artificial intelligence*, volume 37, pages 3543–3551, 2023.

[79] Zhixing Zhang, Bichen Wu, Xiaoyan Wang, Yaqiao Luo, Luxin Zhang, Yinan Zhao, Peter Vajda, Dimitris Metaxas, and Licheng Yu. Avid: Any-length video inpainting with diffusion model. In *Proceedings of the IEEE/CVF Conference on Computer Vision and Pattern Recognition*, pages 7162–7172, 2024.

[80] Yinglin Zheng, Hao Yang, Ting Zhang, Jianmin Bao, Dongdong Chen, Yangyu Huang, Lu Yuan, Dong Chen, Ming Zeng, and Fang Wen. General facial representation learning in a visual-linguistic manner. In *Proceedings of the IEEE/CVF conference on computer vision and pattern recognition*, pages 18697–18709, 2022.

[81] Weizhi Zhong, Chaowei Fang, Yinqi Cai, Pengxu Wei, Gangming Zhao, Liang Lin, and Guanbin Li. Identity-preserving talking face generation with landmark and appearance priors. In *Proceedings of the IEEE/CVF Conference on Computer Vision and Pattern Recognition*, pages 9729–9738, 2023.

- [82] Yi Zhou, Connelly Barnes, Jingwan Lu, Jimei Yang, and Hao Li. On the continuity of rotation representations in neural networks. In *Proceedings of the IEEE/CVF conference on computer vision and pattern recognition*, pages 5745–5753, 2019.
- [83] Hao Zhu, Wayne Wu, Wentao Zhu, Liming Jiang, Siwei Tang, Li Zhang, Ziwei Liu, and Chen Change Loy. CelebV-hq: A large-scale video facial attributes dataset. In *European conference on computer vision*, pages 650–667. Springer, 2022.
- [84] Xiangyu Zhu, Zhen Lei, Xiaoming Liu, Hailin Shi, and Stan Z Li. Face alignment across large poses: A 3d solution. In *Proceedings of the IEEE conference on computer vision and pattern recognition*, pages 146–155, 2016.

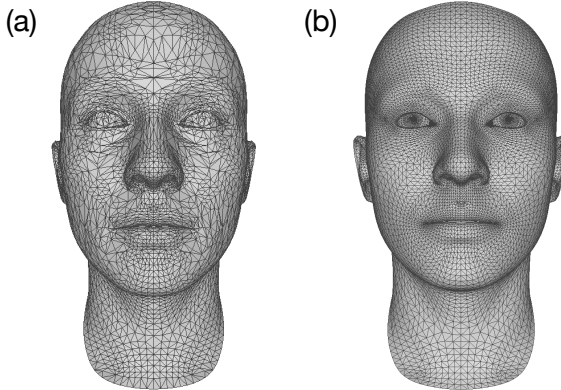


Figure 8: (a) Simplified geometry (b) Original geometry after triangulation.

A 3DMM geometry

We keep only the face and the eyeballs of the ICT-FaceKit. After triangulation, the ICT-FaceKit has 12,549 vertices and 24,852 faces. We further simplify the mesh to have 5,099 vertices and 9,857 faces (as a comparison, the FLAME face mesh has 5,023 vertices and 9,976 faces). The mesh is simplified by using the quadratic mesh error [10], except that we average the error over 50 randomly generated expressions, and decimate vertices symmetrically. The result is shown in Fig. 8. While this simplification is not necessary, it reduces unnecessary compute. Note that we use all of the blendshapes and the first 50 identity parameters of the ICT-FaceKit.

We next give pseudocode for encoding the 3DMM (see discussion in Sec. 3.1 and visualization in Fig. 1) using PyTorch and PyTorch3D. P is computed as follows:

```

1 # B: batch size, N_V: number of vertices, N_T: number of triangles
2 # v_f: vertices in facial coordinates of shape [B, N_V, 3]
3 # mesh: face mesh transformed to world coordinates
4 # rasterizer: pytorch3d rasterizer
5 fragments = rasterizer(mesh)
6 pix_to_face = fragments.pix_to_face # [B, H, W, 1]
7 bary_coords = fragments.bary_coords.unsqueeze(-1) # [B, H, W, 1, 3,
8     1]
9 foreground = (pix_to_face >= 0).permute(0, 3, 1, 2) # [B, 1, H, W]
10 packed_faces = mesh.faces_packed() # [B*N_T, 3]
11 packed_verts = mesh.verts_packed() # [B*N_V, 3]
12 pix_to_verts_idx = packed_faces[pix_to_face] # [B, H, W, 1, 3]
13 P = v_f.view(-1, 3)[pix_to_verts_idx] * bary_coords
14 P = P.sum(axis=-2).squeeze(-2).permute(0, 3, 1, 2)
15 P = P * foreground # [B, 3, H, W]

```

F_{3DMM} is computed as follows:

```

1 # camera: pytorch3d camera
2 # d: driving, r: reference
3 # packed_verts, pix_to_verts_idx, packed_proj_verts,

```

```

4 # bary_coords, foreground are computed as before
5 packed_proj_verts_d = camera.transform_points_screen(packed_verts_d)
6 packed_proj_verts_r = camera.transform_points_screen(packed_verts_r)
7 pix_to_verts_d = (packed_proj_verts_d.view(-1, 3)[pix_to_verts_idx_d]
8     * bary_coords_d.unsqueeze(-1)).sum(axis=-2).squeeze(-2)
9 pix_to_verts_sd = (packed_proj_verts_s.view(-1, 3)[pix_to_verts_idx_d]
10    ] * bary_coords_d.unsqueeze(-1)).sum(axis=-2).squeeze(-2)
11 F_3dmm = (pix_to_verts_sd - pix_to_verts_d) * foreground_d

```

The pseudocode for computing the gaze blendshapes from gaze direction for the right eyeball is as follows:

```

1 # rot_matrix: rotation matrix for right eyeball of shape [B, 3, 3]
2 # th_max, tv_max: maximum horizontal and vertical gaze angles
3 d = rot_matrix[:, 2] # gaze direction
4 th = torch.atan2(d[:, 0], d[:, 2]) # horizontal angle
5 tv = torch.atan2(d[:, 1], d[:, 2]) # vertical angle
6 norm_h = (th / th_max) # normalize horizontal angle
7 norm_v = (tv / tv_max) # normalize vertical angle
8 eye_look_in = norm_h.clamp(0, 1)
9 eye_look_out = -norm_h.clamp(-1, 0)
10 eye_look_up = norm_v.clamp(0, 1)
11 eye_look_down = -norm_v.clamp(-1, 0)

```

Note that x -axis points to the right, y -axis points upwards, and z -axis points out of the plane in Fig. 8. Therefore, when all gaze related blendshapes are zero, the gaze direction points towards the z -axis. The computation for the left eyeball is similar. Note that the maximum gaze angles in the horizontal direction (th_max) and vertical direction (tv_max) are typically set to be around 30° [24].

B Further details on the architecture

ReconNet: We use ResNet-50 backbone [21], except that the head predicts $\alpha \in \mathbb{R}^{50}$; $\beta \in \mathbb{R}^{55}$; $r^h, r^e \in \mathbb{R}^{12}$; $t_{head} \in \mathbb{R}^3$. Note that we use a 6D representation of rotation [25]. The input image, P , and S are all at 224×224 resolution.

FlowNet, Generator. The architecture of FlowNet is adapted from HeadGAN with the following changes:

- InstanceNorm [26] is replaced by GroupNorm [24].
- Input channel is 10 (I, P, S, F_{3DMM}).
- Output channel of first convolution block is 64, instead of 32.

Note that the maximum number of channels is kept at 512, and that input and output resolution are 256. The architecture of Generator is adapted from HeadGAN with the following changes:

- InstanceNorm is replaced by GroupNorm.
- Input channel is 15 (three consecutive P and S).

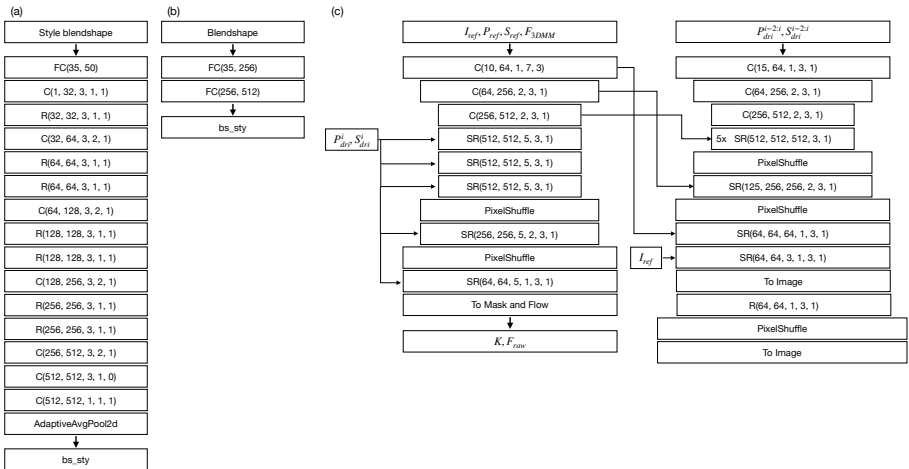


Figure 9: (a) Style Encoder. (b) Blendshape Encoder. (c) FlowNet and Generator. FC represents fully-connected layer with Leaky ReLU activation. C represents simple ConvBlock with group normalization and Leaky ReLU activation. R represents ResBlock. SR represents SPADE ResBlock. The numbers in the parenthesis in C and R are input channels, output channels, kernel size, stride, and padding. The numbers in the parenthesis in SR are input channels, output channels, conditioning channels, kernel size, stride, and padding. In (a), the output is reshaped to $[B, 1, 50, 50]$ after FC. In (c), To Image is a simple ConvBlock with sigmoid activation. To Mask and Flow is also a simple ConvBlock, where Flow has linear activation and Mask has sigmoid activation.

- Output channel of first convolution block is 64, instead of 32.
- The number of SPADE layers at the lowest resolution is increased from 1 to 5.
- We remove AdaIN blocks that use audio signals.

Note that max channel is kept at 512, and that the input and output resolution is 256. See Fig. 9 (c).

Discriminator. The architecture of Discriminator is adopted from HeadGAN, which is similar to that in [43], except for the following changes:

- InstanceNorm is changed to GroupNorm
- Input channel size is 8 (I, P, S)

We use three discriminators, one for the full image, one for the eyes, and one for the mouth.

AudioEncoder. The audio encoder in the Audio-to-Blendshape module is the same as the audio encoder in Wav2Lip [43].

Audio-to-blendshape. The style encoder in the Audio-to-Blendshape module is shown in Fig. 9 (a). The blendshape encoder for computing sync-loss is shown in Fig. 9 (b). The denoising net follows the simple UNet-style convolutional network with cross attention in SAiD [40].

BlendingNet. The BlendingNet is a simple UNet [29, 44]. The output of UNet (I_{pred}) is blended into the original image as follows:

$$I_{blend} = I_{orig}(1 - K_{mouth}) + I_{pred}K_{mouth} \quad (3)$$

C Further details on training

C.1 Pretraining the ReconNet

For faster convergence, we initialize the backbone of ReconNet with a pretrained backbone [8]. We use L2 loss for landmark $\mathcal{L}_{lm} = \|l_{label} - l_{3DMM}\|_2^2$ and the L2 regularization $\mathcal{L}_{reg} = \|\alpha\|_2^2 + \|\beta\|_2^2$. Note that l_{label} consists of 68 standard facial landmarks supplemented by 10 additional landmarks for the iris, which are extracted using MediaPipe [45]. We also include identity consistency loss $\mathcal{L}_{id} = \|\alpha_1 - \alpha_2\|_2^2$, where 1 and 2 indicate identity parameters extracted from the same video but from different frames. Since blendshapes are designed to lie between 0 and 1, we penalize deviations using $\mathcal{L}_{constraint} = \text{mean}(\text{max}(\text{abs}(\beta - 0.5), 0.5) - 0.5)$, where max and abs are element-wise operations. The full ReconNet loss \mathcal{L}_{recon} is a sum of these losses, with the weights given by $\lambda_{lm} = 80$, $\lambda_{reg} = 0.025$, $\lambda_{id} = 0.025$, $\lambda_{constraint} = 0.2$. We train for 100,000 steps using the Adam [29] optimizer with batch size 128, a learning rate of 0.0001, and betas (0.9, 0.999). Training takes about 1.5 days on a single NVIDIA A100 GPU.

C.2 Joint training of ReconNet and Generator

We use the VGG perceptual loss [30, 53] $\mathcal{L}_{perceptual}$ and L1 pixel loss \mathcal{L}_{pixel} on the foreground regions between the ground truth and predicted images. We use the GAN hinge loss [43] \mathcal{L}_{GAN} , along with feature matching loss [54] \mathcal{L}_{FM} . The mask K is guided using L1 loss \mathcal{L}_{FG} to predict the foreground region [54]. We use VGG perceptual loss $\mathcal{L}_{perceptual}^w$

and masked L1 pixel loss \mathcal{L}_{pixel}^w between the warped image and the ground truth image. As auxiliary losses, we use L1 loss between F_{3DMM} and F on the face region to encourage the predicted flow to be consistent with 3DMM. To enforce spatial locality, we detect the mouth region and use L1 loss $\mathcal{L}_{locality}$ to demand that when mouth blendshapes are changed by shuffling the mouth blendshapes within the batch, the generated image does not change outside the mouth region. To disentangle expression from identity and head pose, we shuffle expressions inside the batch and impose the cosine similarity loss $\mathcal{L}_{arc} = 1 - \hat{z}_{arc} \cdot \hat{z}'_{arc}$ between the original face and the reenacted face, where \hat{z}_{arc} is the unit-norm ArcFace [20] embedding. We also randomly shuffle identity parameters between reference and driving images to prevent expression and head pose from leaking into the identity parameters. The loss weights are as follows: $\lambda_{perceptual} = 10$, $\lambda_{GAN} = 1$, $\lambda_{FM} = 10$, $\lambda_{pixel} = 50$, $\lambda_{perceptual}^w = 10$, $\lambda_{pixel}^w = 50$, $\lambda_{FG} = 10$, $\lambda_{locality} = 20$, $\lambda_{arc} = 1$. We also add L2 smoothness loss \mathcal{L}_{smooth} with $\lambda_{smooth} = 0.025$, so that blendshapes, head translations, head rotations, eye rotations between consecutive frames do not change too much.

We train with the Adam optimizer with an initial learning rate of 0.0002, $\beta = (0.5, 0.999)$, and batch size of 80. We train for 150,000 steps, where we reduce the learning rate by half starting from 50,000 steps with an interval of 15,000 steps. Training takes about 4 days on 8 NVIDIA A100 GPUs.

C.3 Audio-to-Blendshape

We predict the denoised blendshapes, so the loss is $\mathcal{L}_{simple} = \|\hat{b}_{0:49}^0 - b_{0:49}^0\|_2^2$. We also include the velocity loss $\mathcal{L}_{vel} = \|(b_{1:49}^0 - b_{0:48}^0) - (\hat{b}_{1:49}^0 - \hat{b}_{0:48}^0)\|_2^2$, and the smoothness loss $\mathcal{L}_{smooth} = \|\hat{b}_{2:49}^0 - 2\hat{b}_{1:48}^0 + \hat{b}_{0:47}^0\|_2^2$. To help train the Audio Encoder, we also include the sync-loss as follows. Recall from Sec. 4.1 that the Mel spectrograms are encoded into $a_i \in \mathbb{R}^{512}$, $i = 0, \dots, 49$. We encode b_i , $i = 0, \dots, 49$ corresponding to a_i into $v_i \in \mathbb{R}^{512}$ using a shallow network (Blendshape Encoder in Fig. 2). The sync-loss is given by

$$\mathcal{L}_{sync} = -\frac{1}{50 \times 2} \sum_{i=0}^{49} \log \frac{e^{\phi(v_i, a_i)}}{\sum_{j \notin \{i-1, i+1\}} e^{\phi(v_i, a_j)}} - (a \leftrightarrow v) \quad (4)$$

During training, we randomly drop the audio signal with probability 0.1, the previous audio with probability 0.5, and the previous blendshape sequence with probability 0.5. The loss weights are $\lambda_{simple} = 1$, $\lambda_{vel} = 7.5$, $\lambda_{smooth} = 1$, $\lambda_{sync} = 1$. The total number of denoising steps T is set to 1000. During inference, we use 50 denoising steps. We train using the AdamW [36] optimizer with betas (0.9, 0.999), a learning rate of 0.0001, and a batch size of 128 for 500,000 steps. Training takes about 2 days on a single NVIDIA A100 GPU. Note that during inference, we use classifier free guidance [23] with the guidance scale fixed to 1.2 for audio and style.

C.4 BlendingNet

We train using $\mathcal{L}_{perceptual}$, \mathcal{L}_{pixel} , \mathcal{L}_{GAN} , \mathcal{L}_{FM} with weights $\lambda_{perceptual} = 10$, $\lambda_{pixel} = 50$, $\lambda_{GAN} = 1$, and $\lambda_{FM} = 10$. We use the Adam optimizer with $\beta = (0.5, 0.999)$, a learning rate of 0.0002, and a batch size of 80. Training is performed for 150,000 steps, where the learning rate is halved starting from 50,000 steps with an interval of 15,000 steps. Training takes about 7 days on 4 NVIDIA A100 GPUs.

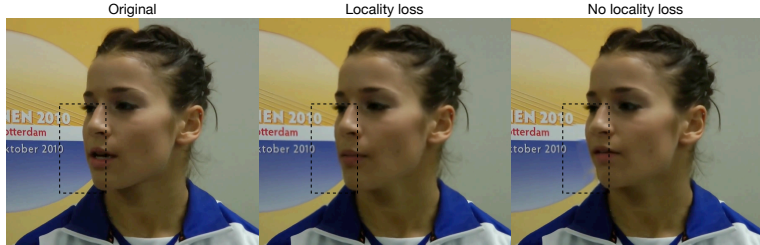


Figure 10: The effect of locality loss. When locality loss is not imposed, visible flickering appears in the background region, which is indicated with a dashed box. This is significantly reduced when the locality loss is imposed.

C.5 Inference Time

When using a single NVIDIA 3090 GPU, the full lip-sync pipeline typically takes around 9 times the duration of the video, where batch size is set to 8 except for the Audio-to-Blendshape model, for which we set the batch size to 1. This includes loading times, the caching time (we cache results such as P and S , I_{FF} , I_{CR} to the hard drive), and the time required to save the final result. Note that mouth mask is created using the face parser provided in FaRL [80].

D Ablation studies

Locality loss. The locality loss is necessary for natural lip-sync. Recall that the locality loss demands that the areas outside the mouth does not change when the mouth blendshapes are changed:

$$\mathcal{L} = \|(1 - K_{\text{mouth}})(I_{\text{pred}}^m - I_{\text{ref}})\|_1. \quad (5)$$

Here, I_{pred}^m is the predicted image when mouth blendshapes are changed, and I_{ref} is the reference image. Without the locality loss, there can be flickering in the surrounding region when the current frame is used as the reference to change the chin contour. This is shown in Fig. 10.

Parametrization of warping. The parametrization of the warping operation in Eq. 2 is crucial for convergence. We have also tried detaching the gradient (stopgrad) for the mask K in Eq. 1:

$$F = \text{sg}(K)F_{\text{raw}}, \quad I_{\text{warped}} = F \star I. \quad (6)$$

We find that this parametrization is more stable than Eq. 1, but even Eq. 6 can cause K to collapse to zero. An example run where we observed this behavior is shown in Fig. 11. Because $K = F = 0$, features are not warped, and the Generator relies on $S_{\text{dri}}, P_{\text{dri}}$ for the face shape, and on unwarped features for face texture. This is neither intended nor helpful for THS. We have not observed this instability when Eq. 2 is used.

Pretraining the ReconNet. We found that when the ReconNet is randomly initialized, jointly training the ReconNet and the Generator does not converge. It is likely that there exist configurations where the joint training converges without pretraining the ReconNet. However, since jointly training the ReconNet and the Generator is computationally expensive, pretraining the ReconNet should still be desirable for faster convergence.

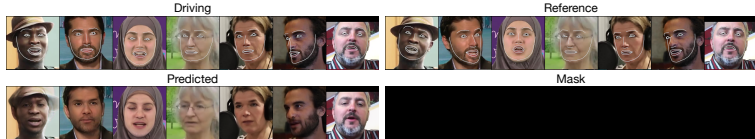


Figure 11: Importance of properly parameterizing the warping operation can be seen from this example run where the mask K collapses to zero. The face sketch S drawn using the 3DMM parameters predicted by the ReconNet is overlaid for reference.

E Further details on evaluation

Self-reenactment. For self-reenactment, we choose the first frame of the video as the reference frame and transfer all of the 3DMM parameters extracted from the video to drive the reference frame. When computing L1, PSNR, and SSIM, we mask out the background because the background region is not of our interest. FID is computed using pytorch-fid [51]. CSIM is computed by averaging all of the ArcFace embeddings for the original video and the generated video.

Cross-reenactment. For cross-reenactment, we select random pairs from the dataset and use the first video to drive the first frame of the second video.

Lip-sync. For lip-sync, we use the pipeline outlined in Fig. 4 of the main text. We would like to note that there is a lip-sync quality gap when the original audio is used for lip-sync and when different audio (audio from a different video in the dataset) is used for lip-sync, see LSE-D and LSE-C in Table 2. We hypothesize that the quality gap is caused by a mismatch between the style blendshapes and the talking style implied by the audio. To understand this phenomenon, let us consider for simplicity just the speaking speed. During training, we sample the style blendshape from a different part of the video, so that the speaking speed is usually similar. However, during inference, the speaking speed between the style blendshapes and the dubbing audio can be quite different, which is probably infrequent in the training data.

F Limitation

Limitations of 2D warping. For the THS, we borrowed the architecture of the HeadGAN framework, which relies on 2D feature warping. Feature warping offers a simple way to achieve temporally consistent video generation because convolutional neural nets are equivariant under translation, and feature warping is locally a translation. However, the 2D warping is weak to occlusions, such as changes in head pose, visibility of teeth, and visibility of iris. This is because it is difficult to encode the information of the occluded area into 2D features. We expect that such limitations can be handled by 3D warping-based methods. Fortunately, this is not difficult to achieve: our preliminary experiments indicate that by binding 3D keypoints to vertices of the 3DMMs, one can incorporate methods based on 3D warping fields into our approach.

Limitations in BlendingNet. We found that our BlendingNet is weak to large changes in illumination. This becomes noticeable when there is strong contrast in the video. We expect that this problem can be addressed by using diffusion inpainting methods, especially video diffusion inpainting methods, which work better than GAN based methods [37, 49, 79].

Limitations of the learned 3DMM parameters. The 3DMM parameters learned in our work is not perfect. For example, it is not 3D consistent because we have not utilized multi-view datasets. The teeth information is also not correctly encoded into the blendshapes. This can be seen by changing the `mouthFunnel` blendshape and the `mouthUpperUp` blendshape. Ideally, the teeth location should be the same when either of the blendshapes is activated, but we find that the teeth location is slightly different in Fig. 5. This problem should also be solvable within our framework by labeling parts of the dataset with teeth landmarks (the full ICT-FaceKit mesh contains teeth), and incorporating these data when computing the landmark loss.

Limitations of identity and expression disentanglement. Although cross-reenactment was not the focus of our work, directly transferring all of the blendshapes from the driving video has limitations in keeping the source frame's identity. This is because it is impossible to completely disentangle expression from identity, especially when using a single image. We expect additional designs for retargeting will be helpful for cross-reenactment [70, 62].

Limitations in capturing detailed expressions. Although some of the detailed expressions, such as wrinkles, can be captured with just the 3DMM (for example, the first row of the self-reenactment results of Fig. 6 in main text), there are limitations. It would be interesting to see if it is possible to supplement the 3DMM with additional features responsible for detailed changes to the face.

Limitations on Audio-to-Blendshape model. As mentioned in Sec. E, the Audio-to-Blendshape model struggles when there is a mismatch between the style blendshapes and the audio. To solve this problem, a more sophisticated treatment of style seems necessary.